MJFAS
Malaysian Journal of Fundamental and Applied Sciences

Abdul Khalil *et al.* | Malaysian Journal of Fundamental and Applied Sciences, Vol. 21 (2025) 2406–2422

RESEARCH ARTICLE

# Optimization of Reduced Graphene Oxide/ Polypyrrole-Coated Fabric via Dip-Coating and *In-situ* Polymerization for Photothermal Application

**Ahmad Faez Abdul Khalil[a], Mohd Haiqal Abd Aziz[a]*, Khoirussolih Aminuddin[a], Muhammad Farid Shaari[b], Ebrahim Mahmoudi[c], Mohammad Arif Budiman Pauzan[d]**

[a]Department of Chemical Engineering Technology, Faculty of Engineering Technology, Universiti Tun Hussein Onn Malaysia, Pagoh Higher Education Hub, 84600, Panchor, Johor, Malaysia; [b]Department of Mechanical Engineering Technology, Faculty of Engineering Technology, Universiti Tun Hussein Onn Malaysia, Pagoh Higher Education Hub, 84600, Panchor, Johor, Malaysia; [c]Department of Chemical and Process Engineering, Faculty of Engineering and Built Environment, Universiti Kebangsaan Malaysia, Bangi 43600, Malaysia; [d]Department of Physics and Chemistry, Faculty of Applied Sciences and Technology (FAST), Universiti Tun Hussein Onn Malaysia (UTHM), Pagoh Campus, 84600, Pagoh, Johor, Malaysia

Abstract Solar-driven interfacial evaporation (SDIE), which utilizes solar absorbers like photothermal fabric, is one of the sustainable and energy-efficient technologies for water treatment particularly suited for off-grid locations and offering high potential for scalable deployment. Employing solar absorbers in the SDIE system enables efficient solar energy harvesting for water treatment, minimizing the dependence on fossil fuels and chemical usage compared to conventional methods. In this study, a cotton fabric coated with polypyrrole/reduced graphene oxide (RGO/PPy) was developed and optimized using response surface methodology (RSM) based on a Box–Behnken design (BBD). The optimization process focused on enhancing the photothermal surface temperature absorption of the RGO/PPy layer for SDIE applications. The optimized theoretical condition (round-off) given are: RGO suspension concentration of 3 mg/mL, pyrrole solution concentration of 0.4 M and a polymerization time of 1 hour. Under these parameters, the fabric predicted can achieve 58.06°C of surface temperature after 20 minutes of exposure. Experimental validation closely matched the predicted result, with observed surface temperatures of 58.07 °C ± 0.06 °C based on triplicate measurements of 58.1 °C, 58.1 °C, and 58.0 °C. This excellent agreement confirms the accuracy and reliability of the optimization process. Materials were characterized using X-ray diffraction (XRD) and Fourier-transform infrared spectroscopy (FTIR). XRD confirmed successful synthesis of the materials, with peaks corresponding to graphite powder, GO, RGO, and PPy observed at specific 2-theta values. FTIR analysis validated the presence of key functional groups, including C=C and C–H stretching vibrations in PPy and oxygen-containing groups in RGO, indicating effective integration onto the fabric. This optimized RGO/PPy-coated fabric was successfully fabricated and exhibited excellent photothermal performance, demonstrating its potential for practical and scalable SDIE applications.

**Keywords**: Reduced graphene oxide, polypyrrole, cotton fabric, solar-driven interfacial evaporation, photothermal, Box-Behnken design.

***For correspondence:**
haiqal@uthm.edu.my

**Received:** 10 May 2025
**Accepted:** 17 July 2025

## Introduction

Environmental pollution and rapidly growing populations have exacerbated freshwater scarcity worldwide. If left unaddressed, global water scarcity is projected to worsen significantly by 2050 with approximately 52% of the world's population expected to live in water-stressed areas due to increasing demand, climate variability and unsustainable resource management [1]. To address this issue, solar steam generation (SSG) via solar-driven interfacial evaporation (SDIE) technology has gained prominence due to its energy efficiency and sustainability [2]. This approach harnesses solar energy to create localized heating at the water–air interface using various photothermal platforms including functionalized fabrics, membranes or composite surfaces to enable efficient water evaporation without external energy sources [3–6]. By using only renewable solar energy, this technology can reduce carbon emissions and suitable for use in off-grid locations. [7]. Furthermore, the design of SDIE systems can be optimized to improve overall performance, increasing their viability for large-scale applications [8–10]. In this system, the photothermal component is essential for capturing solar energy and converting it into thermal energy, while also serving as a water transport layer to ensure continuous water supply to the evaporation surface and maximize the evaporation rate [6,11,12]. Despite growing interest in SDIE systems, the challenge remains in not only identifying efficient photothermal materials but also in formulating and optimizing their concentration and integration techniques to achieve stable, uniform and high-performance solar absorbers.

As shown in Figure 1, the keyword search related to “photothermal” and “evaporation” indicates a strong research interest and interdependence between these two topics, particularly in the context of SDIE systems. The novelty of this research lies not only in the synthesis route but also in the strategic tuning of composite ratios to meet the specific requirements of SDIE applications. It is particularly compelling to explore the synergistic effects of photothermal materials, which remain relatively underexplored. This research direction is further supported by VOSviewer keyword mapping, which highlights a strong co-occurrence of the terms “photothermal” and “evaporation,” reflecting the growing interest in developing photothermal materials specifically for SSG system.

In recent years, many types of materials have been investigated for solar-to-thermal energy conversion applications such as SSG. Among them, 2D carbonaceous materials such as graphene, graphene oxide (GO), and reduced graphene oxide (RGO), which consist of a single layer of carbon atoms arranged in two dimensions, have gained increasing attention due to their unique physicochemical properties [13]. Their versatility, abundance, and strong light–matter interaction make them particularly attractive for efficient photothermal conversion. Carbon-based materials are ideal because they absorb broadly across the solar spectrum, convert light into heat effectively, remain stable at high temperatures. Aside from carbonaceous materials, conducting polymers also have demonstrated remarkable potential as photothermal materials owing to their efficient light absorption, ease of fabrication, and tuneable characteristics. Their ability to harness and convert light into heat makes them highly valuable for diverse applications. Moreover, the synergy between their chemical adaptability, and structural versatility further enhances their performance, allowing precise modulation of optical and thermal properties to suit various technological demands. Nevertheless, when used alone, polymers are often limited by their low thermal conductivity. To address these challenges, they are frequently combined with high-performance nanomaterials like carbonaceous materials. The resulting composites take advantage of the excellent photothermal properties, making them well-suited for advanced applications such as SDIE.

RGO is a prominent candidate material compared to others in SDIE systems due to its exceptional photothermal properties. These materials efficiently convert solar energy into heat and exhibit strong light absorption across the solar spectrum because of its high surface area and porous structure facilitate rapid water transport [14]. RGO was chosen over GO and graphene due to its unique combination of advantages that make it more suitable for the study’s applications. GO, while highly dispersible in solvents due to its oxygenated functional groups, suffers from significantly reduced thermal conductivity because these groups disrupt the $sp^2$ carbon network. This makes GO less effective in applications requiring high thermal performance. On the other hand, graphene exhibits excellent thermal properties but is difficult to disperse in solvents and tends to aggregate, making it challenging to integrate into composites. RGO, which is partially reduced from GO, restores much of the $sp^2$ carbon network, resulting in improved conductivity and photothermal efficiency. RGO also offers better dispersibility than pure graphene, making it easier to incorporate into various systems. Moreover, RGO’s reduced oxygen content enhances its compatibility with conducting polymers, leading to better polymerization and improved composite morphology. This combination of better thermal properties, improved compatibility with polymers, and superior dispersibility makes RGO a more suitable material compared to GO and graphene for the targeted applications in this study.

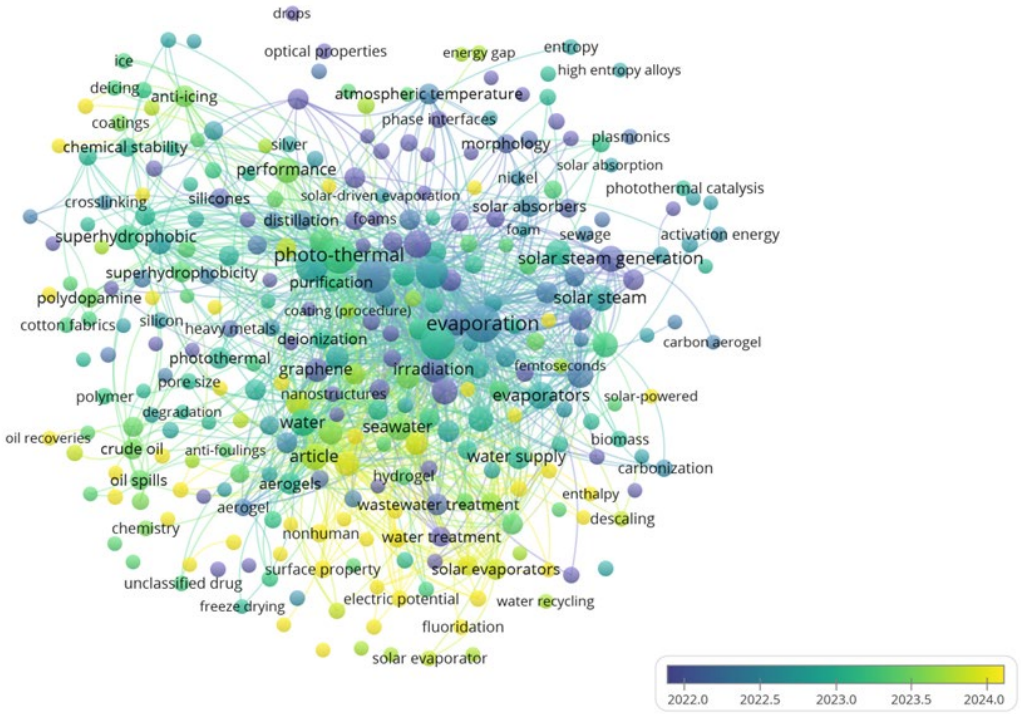


**Figure 1.** Keyword co-occurrence network generated using VOS viewer based on “photothermal” and “evaporation” from 2022 to 2024

Complementing this, polypyrrole (PPy) is a conductive polymer known for its excellent photothermal conversion efficiency and environmental stability [15]. PPy also exhibits strong light absorption and rapid thermal response [15]. The combination of RGO and PPy results in a synergistic hybrid system, where the high thermal conductivity and broad-spectrum absorption of RGO are integrated with the tuneable conductivity, flexibility, and light-responsive nature of PPy. This complementary interaction enhances the overall photothermal performance, making the composite highly suitable for advanced solar energy applications. To boost the evaporation performance of a photothermal component, fine-tuning the material concentrations is essential for an efficient SDIE system to ensure sunlight is effectively converted into thermal energy [16]. This well-dispersed RGO provides a high surface area and strong interfacial interaction during the in-situ polymerization of pyrrole (Py), leading to uniform PPy deposition, improved composite morphology, and enhanced overall performance. Thus, RGO-PPy offers a more effective platform for the development of high-performance photothermal materials.

Previous studies have explored the use of RGO and PPy in photothermal applications, but limited attention has been given to optimizing their concentration ratio and combining methods to enhance both photothermal efficiency and coating stability. Addressing this gap, the present study systematically investigates the effect of varying RGO and PPy concentrations, leading to the development of an optimized composite photothermal layer. A novel two-step fabrication method is introduced, involving dip-coating the fabric with RGO followed by in-situ polymerization of Py. This approach improves coating adhesion, uniformity and overall photothermal performance. The optimized RGO/PPy-coated fabric demonstrates enhanced solar absorption and energy conversion, making it highly suitable for SDIE systems. By leveraging renewable solar energy and advanced materials, this work offers a sustainable and efficient solution for water purification, contributing to the global effort to address freshwater scarcity.

## Materials and Methods

Pyrrole solution (Merck), Iron (III) chloride ($FeCl_3$) (Sigma-Aldrich), synthetic graphite powder (<20 µm) (Sigma-Aldrich), sulfuric acid 95–97% ($H_2SO_4$) (Merck), potassium permanganate (KMnO4) (Bendonsen), 30% hydrogen peroxide ($H_2O_2$) (Merck), 10% hydrochloric acid (HCl) (Merck), ascorbic acid ($C_6H_8O_6$) (Merck) and absolute ethanol (VChem) were supplied by VNK Supply and Services (Johor, Malaysia). The experimental flow is shown in Figure 2 and Figure 3.

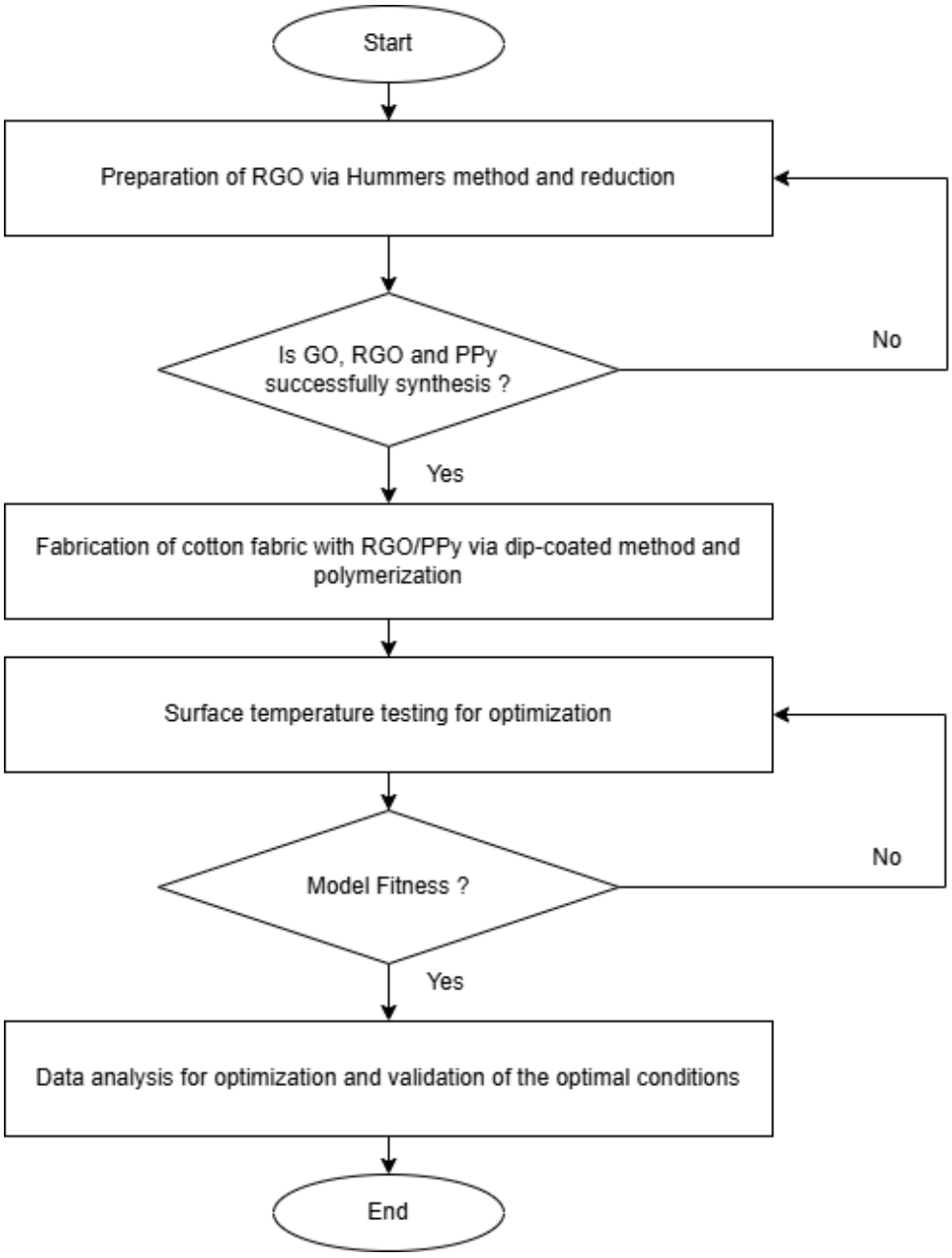


**Figure 2.** Flowchart for the experimental study of RGO/PPy-cotton fabric for SDIE system

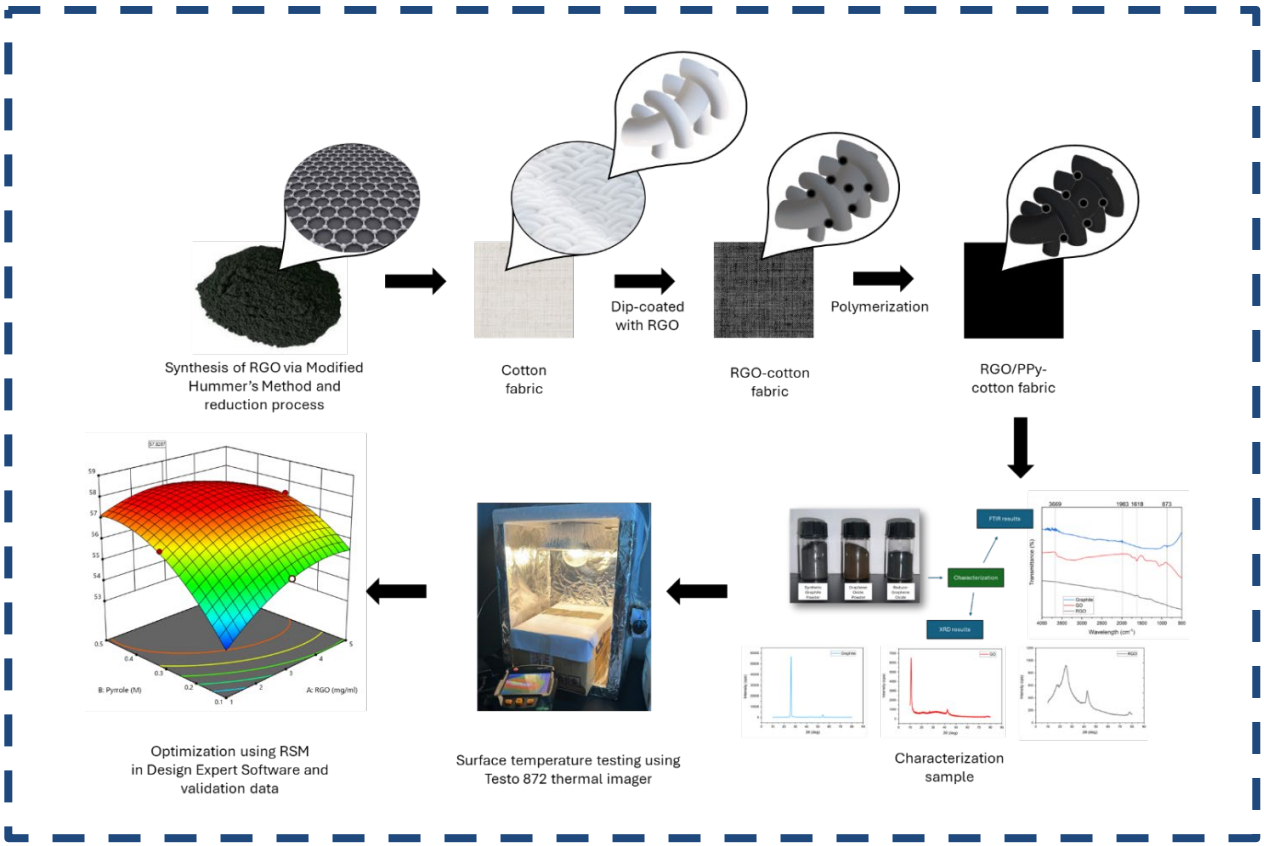


**Figure 3.** Graphical flow for the experimental study of RGO/PPy-cotton fabric for SDIE system

## GO and RGO Powder Preparation

GO was synthesized using a modified Hummers method, as shown in Figure 4(a). First, 23 mL of $H_2SO_4$ was added to a beaker in an ice bath, followed by the gradual addition of 3 g $KMnO_4$ under stirring (500 rpm). After 15 minutes, 1 g synthetic graphite powder was introduced. The mixture was then transferred to a water bath at 35°C and stirred for 1 hour. Next, 50 mL deionized water was added, and the temperature was raised to 80°C for 20 minutes. To stop the reaction, 10 mL $H_2O_2$ was slowly added under an ice bath, turning the solution earthy yellow. The suspension was filtered, washed with 5% HCl and acetone until neutral pH, and dried at 60°C for 24 hours, yielding 1 g GO powder. Then, for GO reduction 1 g GO and 1 g ascorbic acid were dissolved in 100 mL distilled water and heated at 80°C for 30 minutes. The reduced product was collected by vacuum filtration, washed with acetone and deionized water, and dried at 60°C for 24 hours, as shown in Figure 4(b).

## Polypyrrole Powder Preparation

Polypyrrole (PPy) powder was synthesized via chemical polymerization for characterization. A 50 mL 0.5 M pyrrole DI water–ethanol solution (1:1 ratio) was mixed with 50 mL 0.1 M $FeCl_3$ as an oxidizing agent. Polymerization began as the mixture turned from transparent to black. After stirring for 24 hours at room temperature, the product was filtered, washed with deionized water and ethanol, and dried at 60°C for 24 hours before characterization.

## RGO-Cotton Fabric Preparation Via Single Cycle Dip-Coating

A single-cycle dip-coating and drying process in Figure 4(c)(f) was used to fabricate the RGO-coated fabric follow from previous study by Koçanalı *et al*. [17]. Firstly, a 1 mg/mL RGO suspension was prepared using ultrapure water as the solvent prior to the particle size distribution experiments. To obtain well-dispersed solutions, samples were sonicated for 15 minutes. A square cut of untreated cotton fabric with area surface of 25 $cm^2$ was washed, then immediately immersed in the suspension for dip coating for 1 minute to avoid aggregation, followed by drying in an oven at 60°C for 4 hours. After drying, the cotton fabric was washed and dried again three times to check for leaching and ensure coating adhesion. The process was repeated for another sample using different optimized parameters.

## RGO/PPy-Cotton Fabric Preparation

The RGO-fabric prepared in the previous step will be coated with PPy via in situ polymerization as demonstrated in Figure 4(d)(g). The RGO-fabric will be dipped into pyrrole solution with concentration of 0.3 M for 5 minutes. Then, immersed the RGO-fabric in the 0.1 M $FeCl_3$ solution as the oxidant agent to initiate the polymerization process. The fabric will undergo polymerization for 8 hours. After the polymerization is complete, the fabric will be removed and rinsed several times to remove any excess material and dry it in oven for 4 hours at 60°C. As shown in Figure 4(h), RGO/PPy-cotton fabric (optimized sample) were successfully and completely coated. The preparation process was repeated for another sample using different parameters based on the optimization factors.

## Characterization

The elemental identification was conducted using X-ray diffraction (XRD) (Bruker D2 Phaser) analysis from $2\theta = 10^\circ$ to $2\theta = 80^\circ$. Materials used to coat the fabric in powder form were used in the XRD analysis which were graphite, GO, RGO in Figure 4(e) and PPy to make sure the authenticity of the materials coating. The Fourier Transform Infrared Spectroscopy (FTIR) (Perkin Elmer Spectrum Two FTIR Spectrometer) analysis also was run using to confirm that the fabrication of the RGO/PPy-cotton fabric.

## Optimization and Validation Data

The samples were tested using Testo 872 thermal imager under 15,000 Lux intensity for surface temperature analysis. Response surface methodology (RSM) has been used for optimization using Box-Behnken Design (BBD) which is effective for generating robust models while avoiding extreme variable combinations, making it ideal for studies requiring fewer experiments to optimize conditions [18]. The experimental setup and statistical study were executed using Design-Expert software. The BBD three-level, three-factor design was used, comprising of 15 experimental runs. In this study, three variables were included: (A) reduced graphene oxide concentration (mg/ml), (B) pyrrole solution concentration (M) and (C) polymerization time (h), as shown in Table 1. Each variable varied over three levels of -1, 0, +1.

**Table 1**. Box-Behnken design experiment design and factors

| Factor | Code | Level Range | | |
|---|---|---|---|---|
| | | -1 | 0 | +1 |
| RGO suspension concentration (mg/ml) | **A** | 1 | 3 | 5 |
| Pyrrole solution concentration (M) | **B** | 0.1 | 0.3 | 0.5 |
| Polymerization time (h) | **C** | 1 | 4 | 8 |

# Results and Discussion

This section presents a comprehensive performance analysis and thorough characterization of the synthesized materials, including graphite, graphene oxide (GO), reduced graphene oxide (RGO), polypyrrole (PPy), and the RGO/PPy-coated cotton fabric composite. The photothermal properties of the coated fabric were systematically evaluated and optimized, revealing a significant and consistent temperature rise under simulated solar irradiation. The observed photothermal conversion efficiency underscores the material's strong potential for solar-driven interfacial evaporation (SDIE) applications, particularly in water purification systems. Furthermore, the structural, morphological, and chemical transformations associated with the oxidation of graphite to GO and the subsequent reduction to RGO were investigated using X-ray diffraction (XRD) and Fourier-transform infrared spectroscopy (FTIR). These analytical techniques confirmed the successful synthesis of RGO and PPy, as well as their uniform and stable integration onto the cotton fabric matrix. The results validate the effectiveness of the fabrication process and highlight the synergistic interaction between RGO and PPy in enhancing the material's photothermal light absorption and energy conversion.


**Figure 4.** Schematic diagram of (a) Modified Hummer's Method to prepare GO powder. (b) Reduction of GO to RGO using Ascorbic Acid. (c) RGO-coated fabric via dip-coated method. (d) In situ polymerization to fabricate RGO/PPy-fabric. (e) The powder of graphite, GO and RGO that have been obtained. (f) Dip-coated procedure. (g) In situ polymerization of PPy. (h) Comparison between pristine fabric and coated fabric with RGO/PPy (Run 8)

## Characterization

The graphite, GO, RGO, and PPy powder samples were analyzed to confirm the completion of oxidation, reduction, and polymerization reactions and to observe changes in their crystal structure and morphology. The XRD profiles of graphite, GO, RGO, and PPy presented in Figure 5(a) were used to determine their crystalline structures. Graphite exhibits two characteristic peaks at 2θ = 26.4° and 2θ = 54.29° corresponding to the (002) and (004) diffraction planes respectively [17]. Following oxidation, the graphitic peak shifts to 2θ = 10.83° and 2θ = 42.52°. This shift indicates a change in intensity around 2θ ≈ 11°, suggesting an increased inter-planar distance in GO due to the presence of oxygen-containing groups. Additionally, a peak near 2θ = 42.52° reveals the retention of the hexagonal carbon structure, confirming the complete oxidation of graphite to GO [17]. This enlargement is attributed to the incorporation of oxygen-containing functional groups, such as hydroxyl, carbonyl, and carboxyl, into the carbon basal plane during oxidation [17]. Subsequent reduction reactions substantially removed these oxygen-containing groups, leading to the transformation of GO's crystal structure. The XRD pattern of RGO shows a relatively small peak at 2θ = 17.67° (001) and a prominent peak at 2θ = 25.06° (002) as previously described by Chen *et al.* [19]. The peak at 26.62° value for PPy confirming the successful synthesis of the polymer. PPy typically exhibits both amorphous and crystalline regions. The sharpness and intensity of the XRD peak at 26.62° provide insights into the degree of crystalline. A more pronounced peak suggests a higher degree of ordering in the π-π stacking, which can enhance electrical conductivity and mechanical stability [20].

The FTIR spectra in Figure 5(b) shows the progressive changes during the transformation of graphite to GO and RGO. The peak around 3390 $cm^{-1}$ was more pronounced in GO as a sign of oxidation of graphite to GO but significantly reduced in all RGO as a sign of reduction of GO to RGO. The reduced peak (in RGO) also at around 3390 $cm^{-1}$ was more pronounced in RGO using hydrazine as reductant than using acid ascorbic indicating a better reduction using acid ascorbic over hydrazine [21]. Key absorption peaks for GO are observed around 1618 $cm^{-1}$ (C=O stretching) and 1983 $cm^{-1}$ (epoxy groups) indicating successful oxidation of graphite. The characteristic peak at 873 $cm^{-1}$ corresponds to C-H out-of-plane bending vibrations. Upon reduction to RGO, the intensities of oxygen-containing functional group peaks decrease, confirming the partial removal of oxygen functionalities. The disappearance of absorbance peaks of O–H group (3324 $cm^{-1}$), C=O (1737 $cm^{-1}$) and C–O (1312 $cm^{-1}$, 1098 $cm^{-1}$, and 948 $cm^{-1}$) were supported by the data from previous study [22]. This transformation enhances the hydrophobicity and conductivity of the material, crucial for its application in photothermal systems. As shown in Figure 5(c) compares the FTIR spectra of PPy, RGO, pristine cotton, and RGO/PPy-coated cotton (Run 8). The pristine cotton spectrum exhibits characteristic peaks at 3324 $cm^{-1}$ (O-H stretching) and 2899 $cm^{-1}$ (C-H stretching), indicative of cellulose structures. Upon incorporation of PPy and RGO, new peaks emerge such as those at 1737 $cm^{-1}$ (C=O stretching) and 1312 $cm^{-1}$ (aromatic C-N stretching), confirming the successful functionalization of the cotton substrate. The synergistic interaction between PPy and RGO enhances the photothermal properties of the composite as indicated by the additional absorption bands. The broad peak around 3324 $cm^{-1}$ observed in the cotton spectrum corresponds to the O–H stretching vibrations of hydroxyl groups present in cellulose. This peak also was significantly reduced or absent in the RGO/PPy-cotton spectrum, indicating successful surface modification. The disappearance of the O–H peak suggested that the hydroxyl groups on the cotton surface have been masked or chemically interacted with the coated RGO and PPy layers. This can occur due to physical coverage of the surface by the coating or through hydrogen bonding and π–π interactions between the cotton substrate and the nanomaterials. Such changes support the effective deposition of the RGO and PPy layers and confirm the surface modification of the cotton fabric.

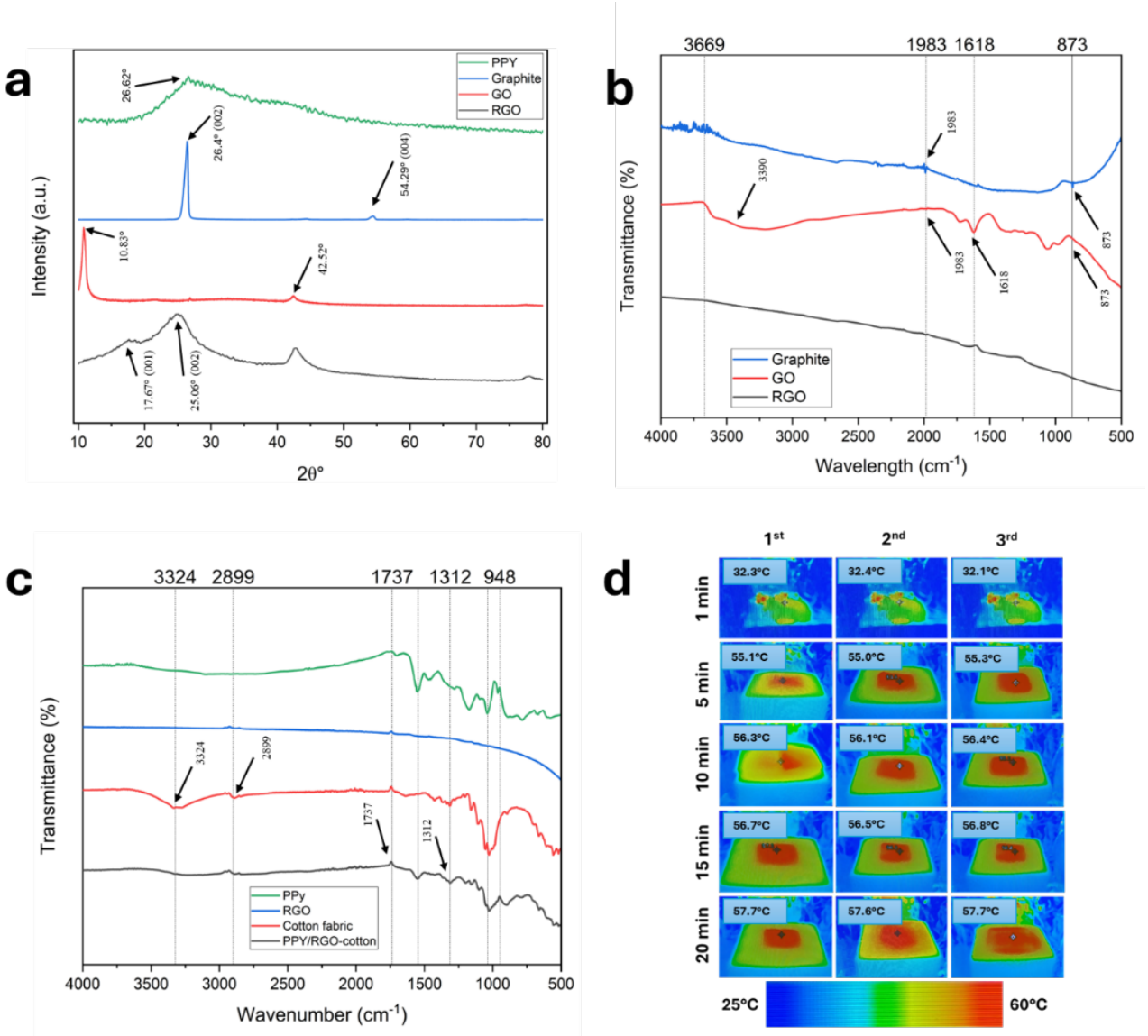


**Figure 5.** (a) XRD materials profile (b) FTIR spectra for graphite, GO and RGO (c) FTIR spectra for PPy, RGO, pristine cotton and RGO/PPy-cotton (d) IR images of surface temperature profile for experimental Run 8'

**Table 2**. FTIR peak interpretation table

| Observed Peak ($cm^{-1}$) | Functional Group | Interpretation | Source |
|---|---|---|---|
| 3390 | O–H / N–H stretch | Broad hydrogen bonding – hydroxyl groups or amine stretch | RGO surface or PPy N–H |
| 1618 | C=C / C=N stretch | Aromatic or conjugated ring vibration | PPy ring or RGO |
| 1383 - 1387 | C–N stretching | C–N or C–H bending | PPy backbone |
| 1324 | C–$N^+$ stretching | Doped nitrogen in PPy | Conductive PPy form |
| 1312 | C–H in-plane bending | Aromatic ring (possibly from PPy or residual organics) | PPy |
| 1737 | C=O stretching | Carbonyl group | Oxidized functional group in RGO |
| 2899 | C–H stretch | Aliphatic C–H (likely minor, possible residual organic material) | Substrate/cotton fabric |

## Optimization and Validation

The surface temperature of the samples was measured using a Testo 872 thermal infrared gun. This test was conducted on all 15 fabric samples to identify the one with the most effective solar absorption and thermal conversion properties. Among them, the RGO/PPy-coated fabric from Run 8 demonstrated the highest surface temperature under simulated solar irradiation, likely due to the synergistic combination of RGO and PPy as shown in the infrared (IR) images in Figure 5(d). The 3 mg/mL RGO suspension provided sufficient surface coverage to enhance light absorption and thermal conductivity without causing agglomeration, which could otherwise hinder photothermal performance. The use of 0.5 M pyrrole enabled uniform and controlled polymerization of PPy, avoiding the structural defects associated with excessive monomer concentration while still achieving good thermal conductivity and film integrity. Additionally, the 1-hour polymerization duration allowed complete but not excessive PPy formation, maintaining a porous and uniform coating. This ensured efficient solar energy absorption and heat localization, while avoiding the formation of overly thick, compact layers that could trap heat or reduce evaporation efficiency. Altogether, these parameters synergistically contributed to Run 8's photothermal response. All the samples fabricated for the experimental design were shown in Figure 6 to visualize the coating and color intensity.

Time-series thermal images revealed a rapid temperature increase during the first five minutes of exposure, followed by a steady rise, eventually reaching a peak average temperature of 57.67 °C at 20 minutes, with a standard deviation of 0.125. This consistent temperature profile, maintained over three heating cycles, highlights the material's excellent stability and photothermal efficiency. The enhanced performance is attributed to the strong light absorption and efficient heat conversion capabilities of the combined PPy and RGO components.

The experimental results are summarized in Table 3. The contour plot in Figure 7(a) shows the interaction effect between pyrrole concentration and RGO suspension concentration on the surface temperature at the 20-minute mark. Similarly, Figures 7(b) and 7(c) illustrate the interactions between RGO concentration and polymerization time, and between pyrrole concentration and polymerization time, respectively. These plots suggest that both RGO and pyrrole concentrations significantly influence the surface temperature, while polymerization time has a less direct impact serving mainly to ensure complete polymerization rather than enhancing thermal performance. For optimization, two key variables which were RGO suspension concentration (mg/mL) and pyrrole solution concentration (M) were varied within defined ranges, while polymerization time was kept minimal based on preliminary findings. The response surface methodology (RSM) as showed in Figure 8 predicted a maximum surface temperature of 58.06 °C under optimal conditions at 3 mg/ml of RGO suspension, 0.4 M of pyrrole concentration and 1 hour of polymerization time. This optimized data supported by the desirability value of 0.919 as shown in Figure 8(a) and coefficient of determination ($R^2$) in Figure 7(d) from the plot Predicted vs Actual, which was 0.9957, indicating that 99.57% of the data variation was accounted by the model.

PPy was incorporated not only for its excellent photothermal properties but also for its ability to enhance thermal conductivity. Its deep black coloration plays a key role in broad-spectrum solar absorption. Darker colors, especially deep black, absorb more light across the solar spectrum compared to lighter shades like grey. Visually, the darker color also qualitatively indicates a thicker coating and a higher loading amount of material. The deep black fabric coating generated higher surface temperature than the grey color coating as state in Table 3 due to its higher color intensity and light absorption. Similarly, RGO improves light absorption, thermal conductivity, and electron transport, further boosting overall efficiency. However, excessive PPy can cause aggregation and reduce mechanical strength, while too much RGO may lead to film cracking and decreased flexibility. Therefore, controlling polymerization time is crucial and it must be long enough to ensure complete polymer formation and strong adhesion, yet short enough to prevent overcoating or structural degradation. Together, the synergistic effects of PPy and RGO, supported by their light-absorbing dark surfaces and carefully tuned processing conditions, play a vital role in maximizing the photothermal performance of the fabric.

The use of RGO in the first step of the two-step coating process also influenced the in-situ polymerization of pyrrole. The RGO-coated surface provided a conductive and textured platform that facilitated the nucleation and uniform growth of polypyrrole during oxidative polymerization. This enhanced the coating adherence and contributed to the synergistic effect between RGO and PPy, ultimately improving the photothermal performance of the resulting composite fabric.

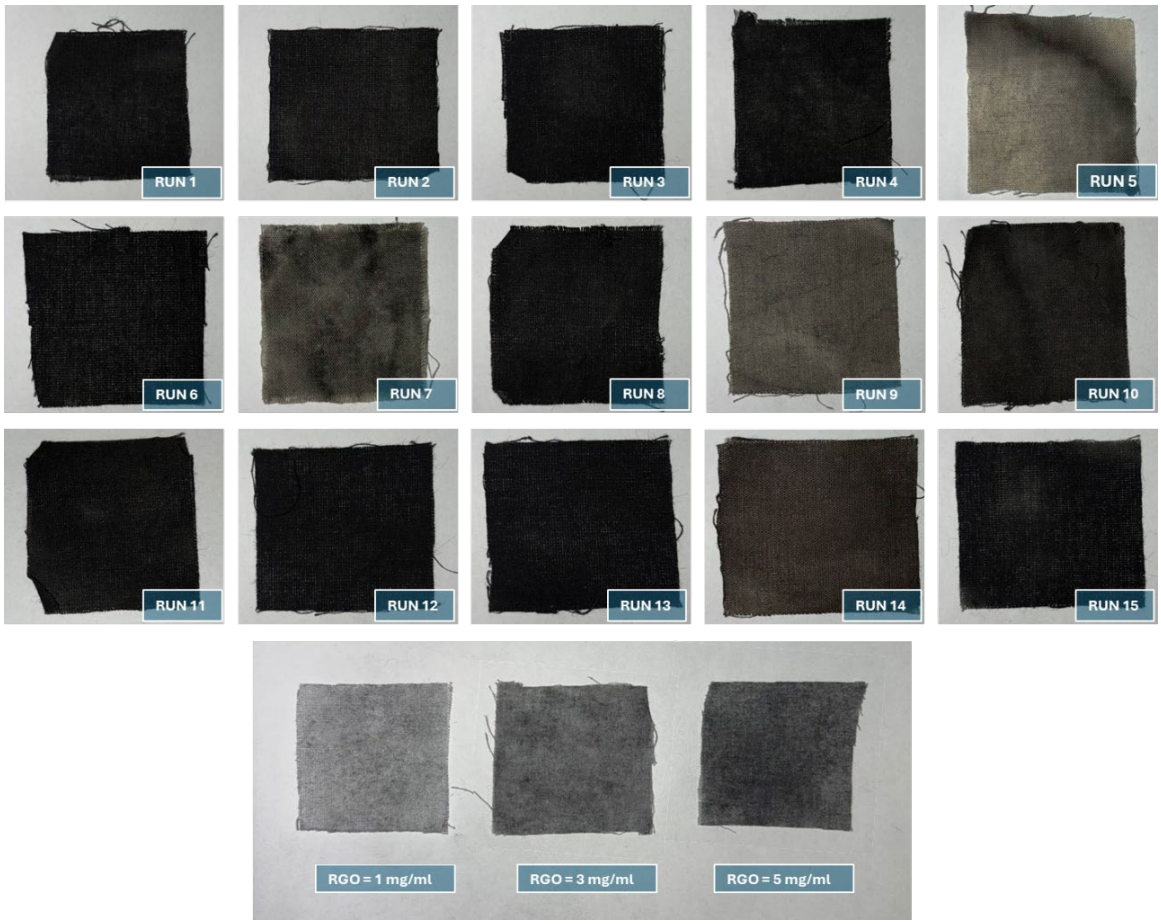


**Figure 6.** Photothermal fabric and control samples from each Design Expert experimental run for photothermal coating

**Table 3**. Experimental response data of of RGO/PPy-fabric for average surface temperature

| Run No. | Level | | | Factor Variables | | | Average Surface Temperature (°C) | | | | |
|---|---|---|---|---|---|---|---|---|---|---|---|
| | | | | Time (min) | | | 1 | 5 | 10 | 15 | 20 |
| | | | | A | B | C | | | | | |
| 1 | -1 | 0 | +1 | 1 | 0.3 | 8 | 32.47 | 53.43 | 55.70 | 56.27 | 56.43 |
| 2 | +1 | 0 | -1 | 5 | 0.3 | 1 | 33.13 | 54.83 | 56.40 | 57.13 | 57.40 |
| 3 | 0 | 0 | 0 | 3 | 0.3 | 4 | 32.83 | 55.30 | 56.07 | 57.20 | 57.50 |
| 4 | 0 | 0 | 0 | 3 | 0.3 | 4 | 32.90 | 55.17 | 56.03 | 57.00 | 57.47 |
| 5 | -1 | -1 | 0 | 1 | 0.1 | 4 | 32.33 | 50.17 | 51.63 | 52.57 | 53.00 |
| 6 | 0 | 0 | 0 | 3 | 0.3 | 4 | 32.93 | 55.27 | 56.40 | 56.97 | 57.27 |
| 7 | +1 | -1 | 0 | 5 | 0.1 | 4 | 32.33 | 50.70 | 52.13 | 53.83 | 54.63 |
| 8 | 0 | +1 | -1 | 3 | 0.5 | 1 | 32.27 | 55.13 | 56.27 | 56.67 | 57.67 |
| 9 | 0 | -1 | -1 | 3 | 0.1 | 1 | 32.90 | 51.27 | 53.27 | 54.70 | 55.20 |
| 10 | +1 | 0 | +1 | 5 | 0.3 | 8 | 32.33 | 53.23 | 54.77 | 55.67 | 55.67 |
| 11 | -1 | 0 | -1 | 1 | 0.3 | 1 | 33.10 | 54.30 | 55.40 | 55.97 | 56.43 |
| 12 | +1 | +1 | 0 | 5 | 0.5 | 4 | 32.03 | 54.67 | 55.63 | 55.80 | 56.40 |
| 13 | 0 | +1 | +1 | 3 | 0.5 | 8 | 31.93 | 55.27 | 56.53 | 57.23 | 57.53 |
| 14 | 0 | -1 | +1 | 3 | 0.1 | 8 | 31.50 | 48.63 | 51.40 | 53.13 | 54.23 |
| 15 | -1 | +1 | 0 | 1 | 0.5 | 4 | 32.23 | 55.13 | 54.93 | 55.57 | 57.47 |

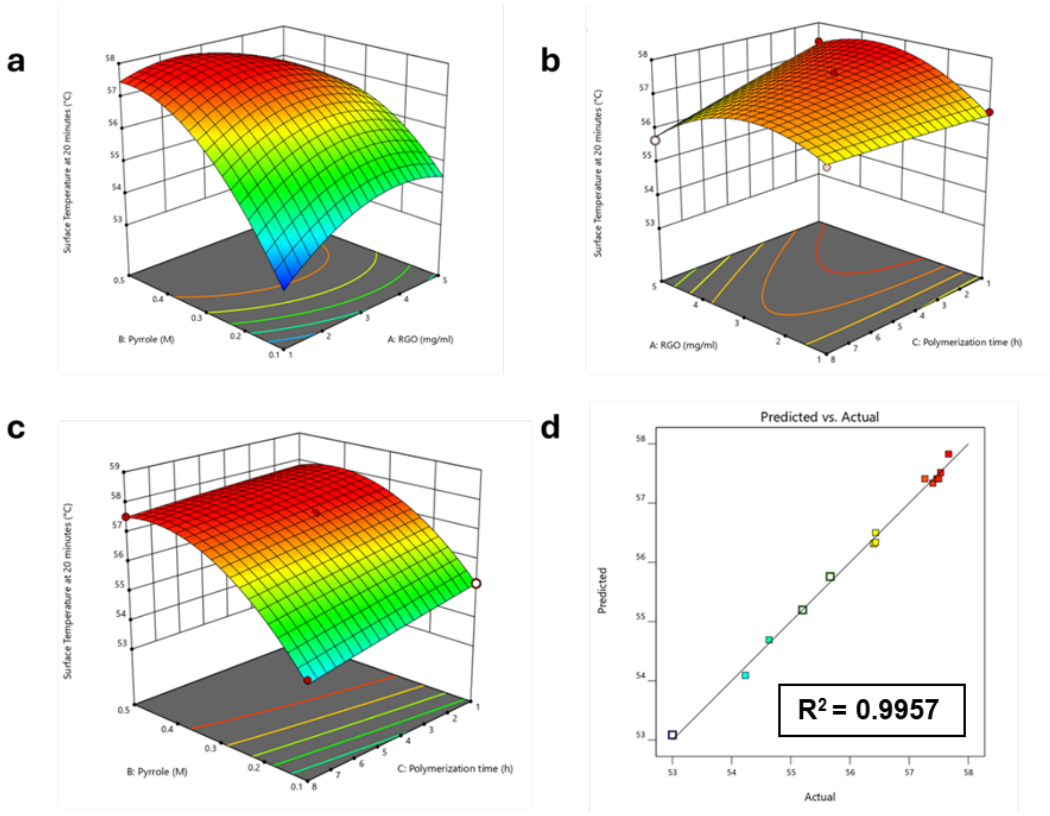


**Figure 7.** Surface plots of the combined a) pyrrole concentration and RGO suspension concentration, b) RGO suspension concentration and polymerization time, c) pyrrole concentration and polymerization time. d) Predicted vs Actual graph

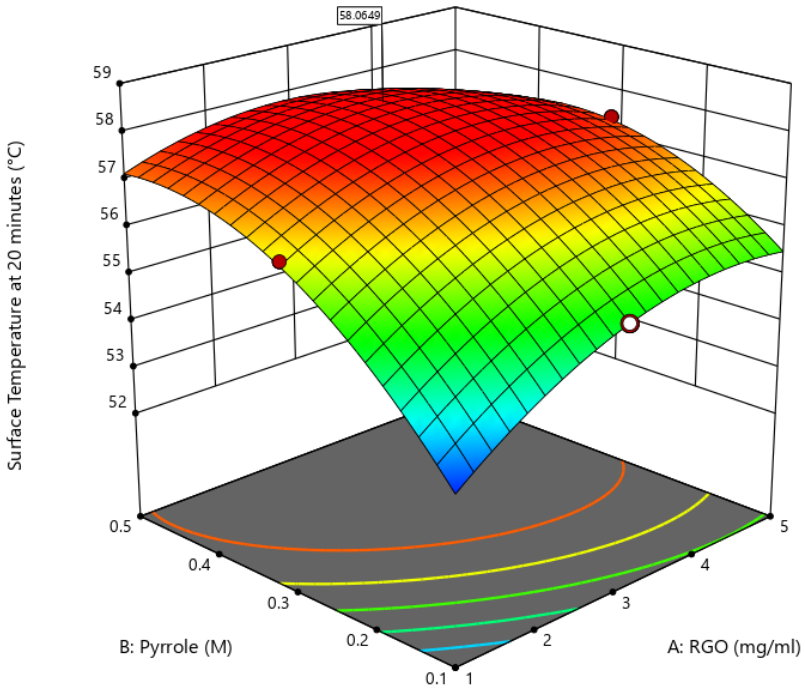


**Figure 8.** Surface plots of the combined pyrrole concentration and RGO suspension concentration

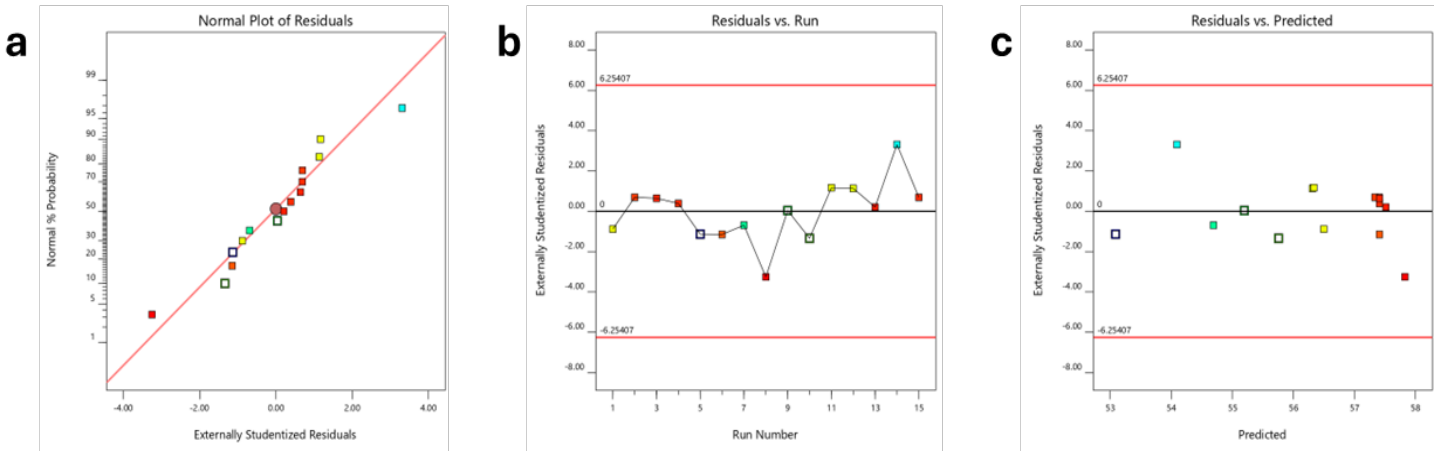


**Figure 9.** Diagnostic graph of a) Normal plot of residuals. b) Residuals vs. run. c) Residuals vs. predicted

The analysis of variance (ANOVA) in Table 4 results revealed that the model is statistically significant, as indicated by the Model F-value of 128.38. This high F-value suggests that there is only a 0.01% probability that such a result could occur due to random noise, confirming the reliability of the model. According to the p-values, which are considered significant when less than 0.0500, the terms B, C, AB, AC, $A^2$, and $B^2$ are identified as significant contributors to the model. Conversely, p-values greater than 0.1000 indicate that the corresponding model terms are not statistically significant. In such cases, excluding non-significant terms that do not affect the hierarchical structure of the model can potentially enhance its predictive performance. As shown in Table 5 for the fit statistic data, the Lack of Fit, F-value of 1.97 suggests that the lack of fit is not significant when compared to the pure error, with a 35.36% probability that such a value could arise due to noise. A non-significant lack of fit is desirable, as it indicates that the model adequately describes experimental data without systematic deviation. The predicted $R^2$ value of 0.9448 is in good agreement with the adjusted $R^2$ value of 0.9879, as the difference between them is less than 0.2. This consistency indicates that the model possesses strong predictive capability and accurately represents the experimental data. The Adequate Precision value, which evaluates the signal-to-noise ratio, was found to be 36.553. Since a ratio greater than 4 is considered desirable, this high value confirms that the model provides a sufficient signal and can be effectively used to explore and optimize the design space.

The diagnostic plots provide important insights into the adequacy and reliability of the regression model. The normal probability plot of residuals in Figure 9(a) shows that the externally studentized residuals generally follow a straight line, indicating that the residuals are approximately normally distributed. This supports the assumption of normality, although slight deviations at the tails suggest the presence of minor outliers, which do not significantly compromise model validity. The residuals versus run plot in Figure 9(b) displays a random scatter of residuals around the zero line across the experimental runs, implying that there is no time-related trend or systematic bias and thus the assumption of independence is satisfied. Meanwhile, the residuals versus predicted values plot in Figure 9(c) reveals no clear pattern or funnel shape, suggesting that the variance of residuals remains relatively constant across all levels of prediction, fulfilling the assumption of homoscedasticity. Although there is a slight increase in residuals at lower predicted values, it does not indicate a serious violation. Overall, the model demonstrates acceptable residual behavior, with no significant issues detected, confirming its suitability for interpreting and predicting the experimental data.

**Table 4**. ANOVA for Quadratic model

| Source | Sum of Squares | df | Mean Square | F-value | p-value | |
|---|---|---|---|---|---|---|
| Model | 29.16 | 9 | 3.24 | 128.38 | < 0.0001 | significant |
| A-RGO | 0.0332 | 1 | 0.0332 | 1.31 | 0.3034 | |
| B-Pyrrole | 18.16 | 1 | 18.16 | 719.43 | < 0.0001 | |
| C-Polymerization time | 1.00 | 1 | 1.00 | 39.76 | 0.0015 | |
| AB | 1.82 | 1 | 1.82 | 72.21 | 0.0004 | |
| AC | 0.7662 | 1 | 0.7662 | 30.36 | 0.0027 | |
| BC | 0.1584 | 1 | 0.1584 | 6.28 | 0.0542 | |
| $A^2$ | 2.70 | 1 | 2.70 | 107.08 | 0.0001 | |
| $B^2$ | 5.15 | 1 | 5.15 | 203.89 | < 0.0001 | |
| $C^2$ | 0.0017 | 1 | 0.0017 | 0.0678 | 0.8050 | |
| Residual | 0.1262 | 5 | 0.0252 | | | |
| Lack of Fit | 0.0943 | 3 | 0.0314 | 1.97 | 0.3536 | not significant |
| Pure Error | 0.0319 | 2 | 0.0159 | | | |
| Cor Total | 29.29 | 14 | | | | |

**Table 5**. Fit Statistics

| | | | |
|---|---|---|---|
| Std. Dev. | 0.1589 | $R^2$ | 0.9957 |
| Mean | 56.29 | Adjusted $R^2$ | 0.9879 |
| C.V. % | 0.2822 | Predicted $R^2$ | 0.9448 |
| | | Adeq Precision | 36.5530 |

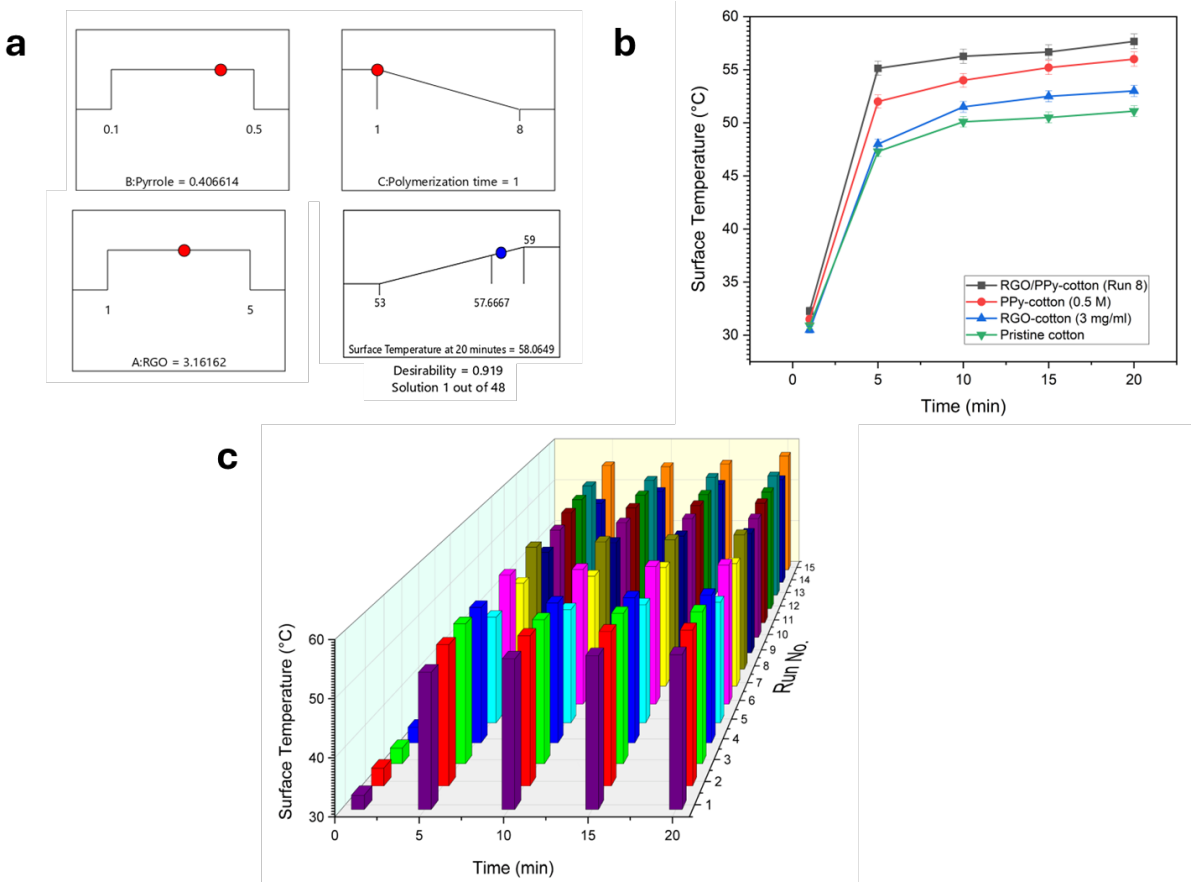


**Figure 10.** a) Optimized conditions for achieving the highest surface temperature. b) Comparison of control samples in surface temperature changes. c) Bar chart showing the average surface temperature for all 15 runs

To validate the accuracy of the mathematical model generated by Design-Expert, as shown by the optimized conditions in Figure 10(a), three experimental trials were conducted again to evaluate the surface temperature, as presented in Figure 11(a). The model predicted a maximum surface temperature of 58.06 °C. The experimental results from the validation runs were 58.1 °C, 58.1 °C, and 58.0 °C, respectively. The average of these three values was 58.07 ± 0.06 °C, which is in excellent agreement with the model prediction. The absolute difference between the model prediction and the experimental mean was only 0.01 °C, corresponding to a relative error of approximately 0.017%. Supported by the preliminary experimental runs in Figure 10(b), the synergistic effect of RGO and PPy enhanced heat absorption compared to coatings of RGO or PPy alone.

In Figure 10(c), all experimental runs were plotted using a 3D bar graph to show the trend. It can be critically observed that the variation in surface temperature across different runs reflects the sensitivity of the system to changes in the synthesis parameters. The bars clearly highlight the impact of RGO concentration, PPy content, and polymerization time on photothermal performance. Runs with optimized conditions show significantly higher surface temperatures, indicating a synergistic effect when the parameters are balanced. This visual representation reinforces the importance of fine-tuning each variable to achieve maximum thermal output and supports the reliability of the optimization process conducted using the Design-Expert model.

All the data plot as bar chart as shown Figure 11(b) for comparative analysis. This extremely low deviation confirms that the model has high predictive accuracy and can reliably be used to estimate the photothermal performance under similar conditions. The minimal variation among the three trials also demonstrates strong repeatability and consistency in the experimental procedure, further validating the robustness of the model.

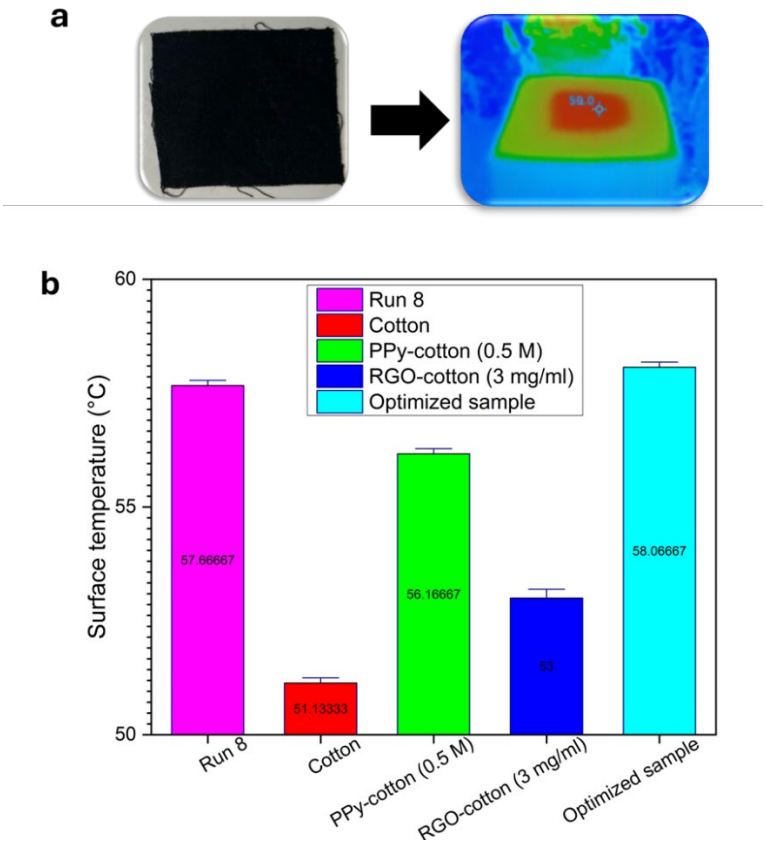


**Figure 11.** a) Validation test for the optimization data (b) Comparison control data with the optimize RGO/PPy-cotton

## Conclusions

In conclusion, this research successfully fabricated reduced graphene oxide/polypyrrole on cotton fabric (RGO/PPy-cotton fabric) as a two-dimensional photothermal material. The highest average surface temperature for experimental run recorded was 57.67 °C under Run 8 and 58.07 °C for optimized condition; RGO suspension concentration of 3 mg/mL, pyrrole solution concentration of 0.4 M and a polymerization time of 1 hour after 20 minutes of solar exposure. Material characterization using XRD and FTIR confirmed the successful synthesis and originality of the components. The unique combination of RGO and PPy demonstrated exceptional photothermal performance, highlighting the capability of the RGO/PPy-coated fabric to efficiently convert solar energy into heat under the optimal condition. The statistical analysis using ANOVA showed a high F-value and a p-value less than 0.05, confirming the significance and reliability of the developed model in predicting surface temperature based on synthesis parameters. These findings demonstrate the potential of using low-cost, flexible fabric substrates for solar-driven interfacial evaporation (SDIE) systems in sustainable water treatment applications. Moving forward, further research is recommended to assess the long-term stability of the material under real environmental conditions, evaluate its water evaporation rate and salt resistance and explore additional functionalities such as antimicrobial or self-cleaning properties. Future studies should also focus on scalability by evaluating the feasibility of large-scale production, conduct durability testing to assess long-term performance under harsh or variable conditions, and explore integration into real-world desalination systems to determine the practical applicability of this photothermal material in off-grid or resource-limited settings.

## Conflicts of Interest

The authors declare that there is no conflict of interest regarding the publication of this paper.

## Acknowledgement

This research was supported by the Ministry of Higher Education (MOHE) through the Fundamental Research Grant Scheme (FRGS/1/2023/TK05/UTHM/02/1). We also want to thank the Government of Malaysia's which provide the MyBrain 2.0 Programme's.

## References

[1] Bañares, E. N., Mehboob, M. S., Khan, A. R., & Cacal, J. C. (2024). Projecting hydrological response to climate change and urbanization using WEAP model: A case study for the main watersheds of Bicol River Basin, Philippines. *Journal of Hydrology: Regional Studies*, *54*, 101846. https://doi.org/10.1016/j.ejrh.2024.101846

[2] Su, J., Zhang, P., Yang, R., Wang, B., Zhao, H., Wang, W., & Wang, C. (2022). MXene-based flexible and washable photothermal fabrics for efficiently continuous solar-driven evaporation and desalination of seawater. *Renewable Energy*, *195*, 407–415. https://doi.org/10.1016/j.renene.2022.06.038

[3] Zhao, X., Zhang, H., Chan, K.-Y., Huang, X., Yang, Y., & Shen, X. (2024). Tree-inspired structurally graded aerogel with synergistic water, salt, and thermal transport for high-salinity solar-powered evaporation. *Nano-Micro Letters*, *16*, 222. https://doi.org/10.1007/s40820-024-01448-8

[4] Huang, Z., Liu, Y., Li, S., Lee, C., & Zhang, X. (2022). From materials to devices: Rationally designing solar steam system for advanced applications. *Small Methods*, *6*(8). https://doi.org/10.1002/smtd.202200835

[5] Ji, Z., Zhao, J., Feng, S., Zhu, F., Yu, W., Ye, Y., & Zheng, Q. (2023). Insight into the charge-ratio-tuned solar vapor generation of polyion complex hydrogel/coal powder composites. *Polymers*, *15*(11), 2449. https://doi.org/10.3390/polym15112449

[6] Xu, X., Zhao, Q., Liu, Q., Qiu, J., Yuan, S., Wu, Z., Yang, R., Cao, J., Wang, L., Xu, J., & Lu, B. (2023). A bilayered wood-poly(3,4-ethylenedioxythiophene):polystyrene sulfonate hydrogel interfacial evaporator for sustainable solar-driven sewage purification and desalination. *Nanomaterials*, *13*(16), 2321. https://doi.org/10.3390/nano13162321

[7] Ye, Z., Zhang, Y., Tian, Z., Chang, Q., Li, N., Xue, C., Hao, C., Yang, J., & Hu, S. (2023). Carbon dots-assisted rapid synthesis of polypyrrole with high uniformity for efficient solar-driven water evaporation. *Advanced Sustainable Systems*, *7*(8). https://doi.org/10.1002/adsu.202300228

[8] Zeng, B., Kumar, T., Wu, H., Stark, S., Hamza, H., Zhao, H., Xu, H., & Zhang, X. (2023). Evolution of morphology and distribution of salt crystals on a photothermal layer during solar interfacial evaporation. *Langmuir*, *39*(42), 14737–14747. https://doi.org/10.1021/acs.langmuir.3c02126

[9] Tian, Y., Yang, H., Wu, S., Gong, B., Xu, C., Yan, J., Cen, K., Bo, Z., & Ostrikov, K. (2022). High-performance water purification and desalination by solar-driven interfacial evaporation and photocatalytic VOC decomposition enabled by hierarchical TiO2-CuO nanoarchitecture. *International Journal of Energy Research*, *46*(2), 1313–1326. https://doi.org/10.1002/er.7249

[10] Chen, S., Zheng, Z., Liu, H., & Wang, X. (2023). Highly efficient, antibacterial, and salt-resistant strategy based

on carbon black/chitosan-decorated phase-change microcapsules for solar-powered seawater desalination. *ACS Applied Materials & Interfaces*, *15*(13), 16640–16653. https://doi.org/10.1021/acsami.2c21298

[11] Chang, C., Liu, M., Li, L., Chen, G., Pei, L., Wang, Z., & Ji, Y. (2022). Salt-rejecting rGO-coated melamine foams for high-efficiency solar desalination. *Journal of Materials Research*, *37*(2), 294–303. https://doi.org/10.1557/s43578-021-00328-w

[12] Chao, J., Lv, B., Zhao, Y., Gong, C., Hong, X., Pan, Y., & Xu, L. (2023). Metal-organic framework-derived carbon materials loading on polydopamine-modified polyurethane foam for interfacial solar steam generation and seawater desalination. *Energy Technology*, *11*(3). https://doi.org/10.1002/ente.202201502

[13] Lagos, K. J., Buzzá, H. H., Bagnato, V. S., & Romero, M. P. (2021). Carbon-based materials in photodynamic and photothermal therapies applied to tumor destruction. *International Journal of Molecular Sciences*, *23*(1), 22. https://doi.org/10.3390/ijms23010022

[14] Wong, M. Y., Zhu, Y., Ho, T. C., Pan, A., & Tso, C. Y. (2023). Polypyrrole-reduced graphene oxide coated delignified wood for highly efficient solar interfacial steam generation. *Applied Thermal Engineering*, *219*, 119686. https://doi.org/10.1016/j.applthermaleng.2022.119686

[15] Hanif, Z., Tariq, M. Z., Khan, Z. A., La, M., Choi, D., & Park, S. J. (2022). Polypyrrole-coated nanocellulose for solar steam generation: A multi-surface photothermal ink with antibacterial and antifouling properties. *Carbohydrate Polymers*, *292*, 119701. https://doi.org/10.1016/j.carbpol.2022.119701

[16] Maity, S., Yadav, M., & Patra, A. K. (2023). Polypyrrole coated textiles as photothermal material for interfacial solar evaporation. *Fibers and Polymers*, *24*(11), 3591–3600. https://doi.org/10.1007/s12221-023-00343-0

[17] Koçanalı, A., & Apaydın Varol, E. (2021). An experimental study on the electrical and thermal performance of reduced graphene oxide coated cotton fabric. *International Journal of Energy Research*, *45*(8), 12915–12927. https://doi.org/10.1002/er.6623

[18] Ferreira, N., Viana, T., Henriques, B., Tavares, D. S., Jacinto, J., Colónia, J., Pinto, J., & Pereira, E. (2023). Application of response surface methodology and Box-Behnken design for the optimization of mercury removal by Ulva sp. *Journal of Hazardous Materials*, *445*, 130405. https://doi.org/10.1016/j.jhazmat.2022.130405

[19] Chen, P., Liu, Y., Zhang, W., Shang, J., & Li, Z. (2020). Preparation of P-reduced graphene oxide composites by one-step hydrothermal method as stable electrode materials. *Chemical Physics Letters*, *754*, 137605. https://doi.org/10.1016/j.cplett.2020.137605

[20] Wang, Y., Song, R., Li, L., Fu, R., Liu, Z., & Li, B. (2021). High crystalline quality conductive polypyrrole film prepared by interface chemical oxidation polymerization method. *Applied Sciences*, *12*(1), 58. https://doi.org/10.3390/app12010058

[21] Faniyi, I. O., Fasakin, O., Olofinjana, B., Adekunle, A. S., Oluwasusi, T. V., Eleruja, M. A., & Ajayi, E. O. B. (2019). The comparative analyses of reduced graphene oxide (RGO) prepared via green, mild and chemical approaches. *SN Applied Sciences*, *1*(9), 1181. https://doi.org/10.1007/s42452-019-1188-7

[22] Maharsi, R., Arif, A. F., Ogi, T., Widiyandari, H., & Iskandar, F. (2019). Electrochemical properties of TiOx/rGO composite as an electrode for supercapacitors. *RSC Advances*, *9*(48), 27896–27903. https://doi.org/10.1039/C9RA04346B